Incoherent Thomson scattering diagnostic development for plasma propulsion investigations

IEPC-2017-442

Presented at the 35th International Electric Propulsion Conference
Georgia Institute of Technology – Atlanta, Georgia – USA
October 8–12, 2017

Benjamin Vincent*, Sedina Tsikata†, George-Cristian Potrivitu‡, and Stéphane Mazouffre§
CNRS, ICARE, 1C ave. de la Recherche Scientifique, 45071 Orléans, France

Incoherent Thomson scattering (ITS) has been applied for decades for the determination of electron density and temperature in fusion plasmas. In recent years, this diagnostic approach has been increasingly extended to studies in low-temperature plasmas. In this work, the design and preliminary implementation of a new, sensitive and uniquely compact ITS platform known as THETIS is described. The diagnostic validation procedures and preliminary results obtained using a hollow cathode plasma source are described. The new tool is intended for application to a range of sources, including Hall thrusters, planar magnetrons and electron cyclotron resonance plasmas.

I. Introduction

The complex physics of plasma sources can be attributed to the presence of charged particles, which act under the influence of electric and magnetic fields and, in turn, generate non-linear effects such as turbulence and energy transfer. The challenge of understanding the particle dynamics in plasma sources has occupied researchers for decades. Yet more fundamental challenges, such as the determination of the particle properties (such as density and energy) remain equally important.

A number of diagnostic tools are available for the determination of electron properties. Electrostatic probes such as Langmuir probes[24,29] are inserted directly into the plasma and their current-voltage characteristics are measured to determine the electron temperature and density. However, such tools have certain shortcomings, such as plasma perturbation and probe damage in regions of high particle density and temperature. Available probe theories are also not adequate for use in magnetized plasma regions.[20]

Non-invasive techniques such as optical emission spectroscopy (OES)[13,14] and interferometry[31,42] are also available. OES involves the analysis of spectral lines of excited species to obtain information on the electron temperature and electron energy distribution function (EEDF). While simple to implement, it relies on complex collisional-radiative[3,19] models (requiring highly-accurate knowledge of cross-sections, difficult to obtain for many gases, and the assumption of Gaussian electron energy distributions) or corona equilibrium models (which rely on the assumption of a low concentration of excited states). Interferometry relies on relating the electron density to a phase shift occurring when incident radiation traverses a plasma. Like OES, it is a line-of-sight measurement, however, localized measurements of spatially-varying electron properties are often required.

Incoherent Thomson scattering (ITS),[23] the focus of this work, was first described in the works of Peacock[36] and Artsimovich[1] in the 1960s. It has a long history of successful application in fusion devices, for example, in Refs. 21,25,28,35, for the determination of electron density and temperature. It offers important advantages in comparison to existing electrical and optical techniques: it is non-invasive, produces direct information, and allows for spatially-resolved measurements. Applying this technique in low-temperature

*PhD student, CNRS, ICARE, benjamin.vincent@cnrs-orleans.fr
†Researcher, CNRS, ICARE, sedina.tsikata@cnrs-orleans.fr
‡Engineer, CNRS, ICARE, george-cristian.potrivitu@cnrs-orleans.fr
§Director of research, CNRS, ICARE, stephane.mazouffre@cnrs-orleans.fr

plasmas is a challenge due to the low plasma densities encountered in such environments (down to 10^{16} m^{-3}), resulting in low scattered signal intensities. This diagnostic is more complex and costly than the other methods described.

Over the last two decades, this technique has been extended to a larger range of plasma sources by several different authors, as seen for instance in Refs. 5–7, 10, 12, 39, 45. These different sources are characterized by electron temperatures on the order of a few eV and electron densities ranging from about 10^{16} - 10^{21} m $^{-3}$. Recently, ITS has been attempted on propulsion plasmas[48,49] and different implementations of the technique are being explored.[15]

In this work, we describe the design and preliminary implementation of a compact new ITS tool destined for measurements in sources such as Hall thrusters,[50] hollow cathodes,[11] planar magnetrons[26] and electron cyclotron resonance sources,[43] among others. This development meets an important need. In Hall thrusters, for example, while a large body of probe measurements exist, such measurements are not considered reliable in the magnetized near-field region of the plasma. This hinders a physical understanding of such regions, where ion acceleration occurs and key instabilities develop. The development of a suitable incoherent Thomson scattering diagnostic for the measurement of electron properties is therefore essential to the future progress in the field.

The new diagnostic has also been designed as a complementary tool for use with another unique diagnostic, PRAXIS.[40] The PRAXIS diagnostic is a highly-sensitive coherent Thomson scattering bench developed in recent years specifically for microturbulence studies in low-temperature plasmas. It has been recently applied for the identification and characterization of instabilities such as the electron cyclotron drift instability in Hall thrusters[9,40] and planar magnetrons.[41] The combination of incoherent and coherent Thomson scattering diagnostics would provide access to highly-detailed information, hitherto unavailable, on electron behavior in many low-temperature sources.

Section II presents the main features of the new diagnostic and its key components. The diagnostic calibration and spectrum analysis procedures are outlined in Section III. Section IVpresents results from the first diagnostic experimental implementation on a hollow cathode plasma source, and conclusions are presented in Sec. V.

II. Diagnostic description

Thomson scattering involves the scattering of incident electromagnetic radiation on free charged particles. Two scattering regimes[16] involving free electrons are denoted according to a scattering parameter α, with $\alpha = 1/k\lambda_{De}$. k is the scattering wavenumber and λ_{De} the electron Debye length. For $\alpha > 1$, the scattering regime is termed collective or coherent: scattered radiation is recovered at length scales larger than the Debye length, and thus collective electron fluctuations are visible. For $\alpha << 1$, the scattering regime is incoherent. The scattered intensity in this latter case is the sum of the contributions from the individual electron scatterers. It reflects the electron density (via the total number of scatterers) and temperature (or, more generally, the electron velocity distribution function (EVDF), via the Doppler shift of the frequency of the scattered radiation due to the electron motion). This work focuses on the incoherent scattering regime.

The main features of the diagnostic design are presented in this section. The new diagnostic is named THETIS (*THomson scattering Experiments for low Temperature Ion Sources*). The optical bench is set up according to the schematic shown in Fig. 1. A top view of the bench and its installation for cathode investigations in the NExET vacuum vessel (length 1.8 m, diameter 0.8 m) are shown. This vessel is equipped with primary, turbomolecular and cryogenic pumps to maintain a minimum pressure of 10^{-7} mbar. The initial laser beam trajectory of the transmission branch is shown in dark green, and the detection branch laser beam trajectory is shown in light green. The plasma volume is indicated in blue. The optical bench is highly compact, with dimensions of 1.5 × 0.75 m.

A. Transmission branch

A number of requirements are taken into account for the performance of the transmission branch. A high level of incident radiation is required (while avoiding processes such as photo-ionization and plasma perturbation[8] due to high power densities in the observation volume). Reflections which could obscure the Thomson scattering signal or damage the detector are to be minimized.

The transmission branch uses a Quantel Nd:YAG laser (Q-Smart 850) which is frequency-doubled for

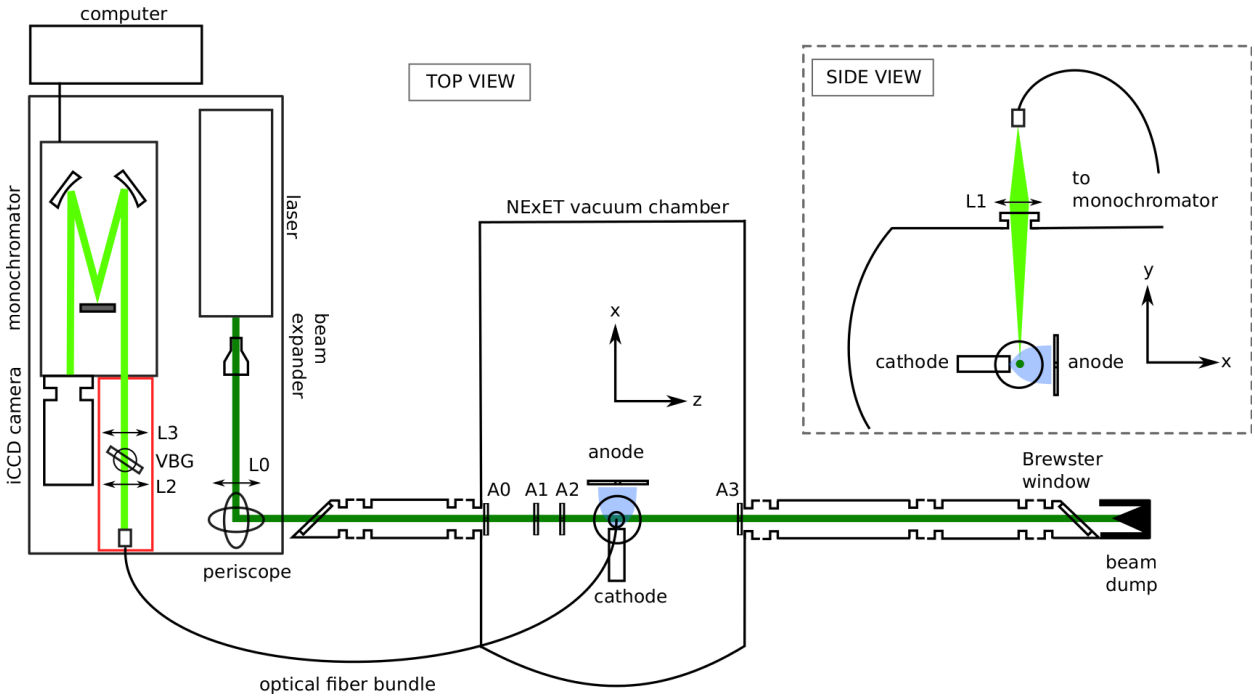

Figure 1. View of the THETIS incoherent Thomson scattering bench setup (not to scale). Two views are shown: a top view of the bench and laser beam trajectory (in dark green) and a side view, showing the collection of scattered light (in light green) at the top of the vacuum vessel. $L0$, $L1$, $L2$ and $L3$ indicate lenses; $A0$, $A1$, $A2$ and $A3$ indicate apertures; VBG indicates the volume Bragg grating used for Rayleigh and stray light suppression. The plasma volume is shown in blue.

operation at 532 nm (with a pulse width of 6 ns, repetition rate of 10 Hz, nominal pulse power of 430 mJ, and an initial beam diameter at the exit of the laser cavity of 9 mm). This choice of wavelength was made due to the availability of high-efficiency detectors and optics with high transmission at 532 nm. The brand of laser was chosen for compactness, high pulse power and stability. As with other Thomson scattering setups, the use of a pulsed, rather than continuous, operation laser provides high-intensity radiation for scattering, the option of time resolution, and the ability to limit collection of stray scattered light.

The initial beam is sent to a beam expander which increases the diameter by a factor of 3 (in order to reduce the beam divergence), and then transmitted to a lens $L0$ (50 mm diameter, focal length 2000 mm, reflectance $R < 0.25\%$ at 532 nm) for focusing in the observation volume of the plasma chamber. Dielectric mirrors in a periscope assembly, treated for a reflectance of 99.6% at 532 nm, are used to transmit light to the observation volume.

The entering beam is polarized in the horizontal xz plane (with $> 80\%$ of the incident optical power along the x direction). The vacuum chamber is equipped with custom fused silica Brewster windows (100 mm minor diameter) mounted at the end of aluminium tubes (total lengths 0.8 and 1.3 m in the current implementation). The use of long tubes for the mounting of the Brewster windows limits the propagation of reflections to the measurement volume.

As seen in Fig. 1, a number of apertures have been set up between the entering laser beam, starting at the vessel wall and up to the plasma volume, with a last aperture at the second vessel wall. These elements, identified by $A0$, $A1$, $A2$ and $A3$ in Fig. 1, are intended to minimize the propagation of stray light reflections (originating from reflections on optical components such as windows). The vessel apertures are constructed from thin metal sheets and diaphragms with matte black coatings. In the center of the plasma volume, the beam waist is 0.3 mm. After traversing the plasma, the beam is sent to a beam dump with a large acceptance aperture (66 mm diameter) which provides multiple internal reflections, limiting the return of dumped light to the vessel.

B. Detection branch

Increasing the incident laser power indefinitely to maximize the Thomson scattered intensity is not feasible, due to the resulting plasma perturbation. With this constraint, the detection branch is designed to recover the maximum number of photons by limiting optics losses as much as possible (for example, by reducing the number of optics elements).

Scattered radiation is recovered perpendicular to the initial beam line, in the y direction, as seen in Fig. 1. Here, a 100 mm-diameter plano-convex lens $L1$ of 200 mm focal length ($R < 0.25\%$ at 532 nm) placed at the top exit port of the vacuum vessel is used to recover the radiation and focus the light onto the end of a fiber bundle. In the side view image (inset), the distance between $L1$ and the center of the plasma is 520 mm; the lens and fiber bundle end are separated by 325 mm.

1. Fiber bundle

A custom fiber bundle is used to relay light collected from the scattering volume to a spectrometer. This fiber bundle is composed of 45 fused silica fibers ($NA = 0.22 \pm 0.02$) of diameter 300 μm, stacked in a 15 $\times$ 3 matrix on one end and a 45 $\times$ 1 matrix at the other. The use of fiber arrays to collect scattered light has been performed by other authors, for example, in Ref. 46.

The use of such a fiber bundle has certain advantages for the setup. It is possible to maximize collection of the scattered light while still providing an easily-adjustable spatial resolution of the observation region (obtained by changing the number of collecting fibers). The stacking used for collection (15 $\times$ 3) allows for easy recovery of the scattered light and is robust to misalignment, while the 45 $\times$ 1 configuration at the spectrometer end allows for measurement within a narrow spectrometer slit of 300 μm. The use of a fiber bundle also simplifies the mounting of the detection branch. All of these advantages are important for the goals of our diagnostic, which is specifically designed for ready installation on a variety of vacuum chambers and plasma sources.

In the current implementation, light from the scattering volume is focused onto a reduced number of fibers (15 fibers) by the lens $L1$. Taking into account the system magnification (a factor of 0.625), the fibers imaged (5 $\times$ 3 matrix) and the beam waist (0.3 mm), this gives a plasma observation volume of 1 mm^3. The signal from all 15 imaged fibers is summed to compose a scattered spectrum.

2. Volume Bragg grating

In addition to the use of apertures for the reduction of stray light, our setup possesses a unique feature: a spectrally-narrow, Volume Bragg Grating (VBG) filter used to significantly attenuate light at 532 nm (composed of stray light and Rayleigh-scattered light on molecules).

Such gratings produce dispersion of wavelengths via their variable refractive indices. Our setup uses one such recently-developed grating from OptiGrate, with an exceptionally narrow bandstop spectral range (full width at half maximum of 0.3 nm), providing an optical density of 4 at 532 nm when correctly aligned. These characteristics are exploited for the attenuation of the signal at 532 nm.

The filter used, identified by VBG in Fig. 1, is placed between lenses $L2$ and $L3$, both of focal length 100 mm and diameter 25.4 mm. The focal lengths and positioning of these lenses are chosen to correctly collimate the light entering the filter and transmit it within the spectrometer's acceptance angle. The filter is mounted on a rotation stage which enables fine adjustments of the filter orientation with respect to the incoming collimated beam.

To our knowledge, this is the first such implementation of the volume Bragg grating filter for stray light attenuation in a Thomson scattering setup. Our design possesses advantages over standard setups which employ double- or triple-grating spectrometers with masks for attenuation of radiation at 532 nm. The transmission efficiency of the VBG outside the narrow bandstop region typically exceeds 90%. For a standard triple grating spectrometer (with coatings for the UV-VIS range), transmission efficiency can range between about 30 - 45% at best. Our use of the VBG filter element also guarantees the compactness of the optical bench. This is, again, a critical feature of a diagnostic intended for diverse implementations.

The use of the Bragg volume grating requires high-quality collimation of the light from $L2$ (only a divergence on the order of 0.1° or less is permissible for adequate attenuation). In our setup, we are presently limited to a filter with a clear aperture of 11 $\times$ 11 mm, for reasons of cost at the time of mounting of our prototype. This results in the loss of some radiation which falls outside the filter dimensions. This point

is discussed further in Sec. F. However, the use of such a component is a step forward for the flexibility and performance of such Thomson scattering platforms. In recent years, gratings of this type have been successfully implemented by other teams for Raman scattering experiments.[27,33]

3. Spectrometer and camera

Unlike many other Thomson scattering setups using double- or triple-spectrometers, this setup uses a single spectrometer. The spectrometer (a Princeton Instruments Acton SP-2750, f/9.7) is fitted with silver-coated mirrors (reflectivity in the visible spectrum $> 98\%$). It uses one of two gratings: either a ruled grating (600 lines/mm), or a blazed holographic grating (2400 lines/mm). These gratings have been selected, respectively, to cover the spectral width expected at high temperatures (tens of eV) and provide adequate wavelength resolution at low electron temperatures (a few eV).

A Princeton Instruments iCCD PI-MAX 4-1024f camera is used for radiation detection and is triggered using the laser Q-switch signal. Its Gen II intensifier has a quantum efficiency of 10% at 532 nm. The front-illuminated CCD dimensions are 13.3 $\times$ 13.3 mm (with pixels of size 13 $\times$ 13 μm). Together, the spectrometer and camera features provide a wavelength coverage of 5.9 nm and 28.7 nm, respectively, for the 2400 lines/mm and 600 lines/mm grating. For the minimum slit width of the spectrometer (highest resolution), the narrowest signal is 3 pixels wide. This corresponds to a maximum resolution of 0.09 nm for the 600 lines/mm grating and 0.018 nm for the 2400 lines/mm grating.

The camera and spectrometer are controlled simultaneously using the same Princeton Instruments LightField program, which allows for the choice of grating, acquisition parameters and the storing of the acquired spectra. Nanosecond gated operation is applied for the camera; this contributes to the attenuation of light at 532 nm by limiting the collection of stray light from optics far from the observation volume, and by limiting the accumulation of the plasma emission.

III. Spectrum analysis procedures

The use of the ITS diagnostic requires appropriate calibration to determine the absolute electron density, using either Rayleigh scattering or Raman scattering.

An electromagnetic field incident on a molecule induces an oscillating dipole, and the nature of energy re-emission determines the type of scattering. For molecules at rest with energy re-emission at the same frequency as the incident radiation, the scattering is of the (elastic) Rayleigh type. On the other hand, if the energy absorption causes a change of the vibrational or rotational state of the molecule, scattering is of the (inelastic) Raman type. Resonance Raman scattering is also associated with changes in the electronic state of the molecule.

In Raman scattering, the molecule may emit photons of lower energy than the incident photon (in which case the corresponding emission lines are at wavelengths above the incident wavelength). On the other hand, the molecule, if previously in an excited state, may emit photons of higher energies than the incident photons, resulting in spectral emission lines at lower wavelengths than the incident radiation.

A. Instrument function characterization

Prior to the diagnostic calibration, it is necessary to determine the instrument function of the detection branch under the same acquisition parameters and configuration as those intended for the calibration and Thomson spectra.

Determination of the instrument function is done by pumping down the vacuum vessel to its lowest pressure to remove residual gas (which could contribute to Raman or Rayleigh scattering) and sending the laser beam across the vessel to provide an artificially-large level of stray light at 532 nm (for example, using a reflective object). This signal is collected by the detection branch. A similar measurement is then made with the laser off, for the same duration; this constitutes the background noise. The instrument profile is determined from the difference between these two spectra.

The instrument function profile is normalized such that $\Sigma I(\lambda)\delta\lambda = 1$, where $I(\lambda)$ is the intensity (in photodetector counts) and $\delta\lambda$ is the wavelength step. This normalized instrument function will be convolved with theoretical calibration spectra to account for the actual redistribution of the monochromatic light intensity over the pixels; such a redistribution is a consequence of the specific features of the detection branch. This redistribution is assumed to be constant over the spectral interval probed. Since the spectral

width of the monochromatic light is negligible in comparison to the instrument function width, it is therefore considered to be a Dirac function in its convolution with the instrument function.

Fig. 2 shows the normalized instrument functions determined for the usual experimental slit width for two cases: with a single pixel (in the absence of horizontal pixel binning), and with binning over 8 horizontal pixels. With no binning, the FWHM of the instrument function peak is 0.06 nm; with binning over 8 pixels, the instrument function width is 0.12 nm.

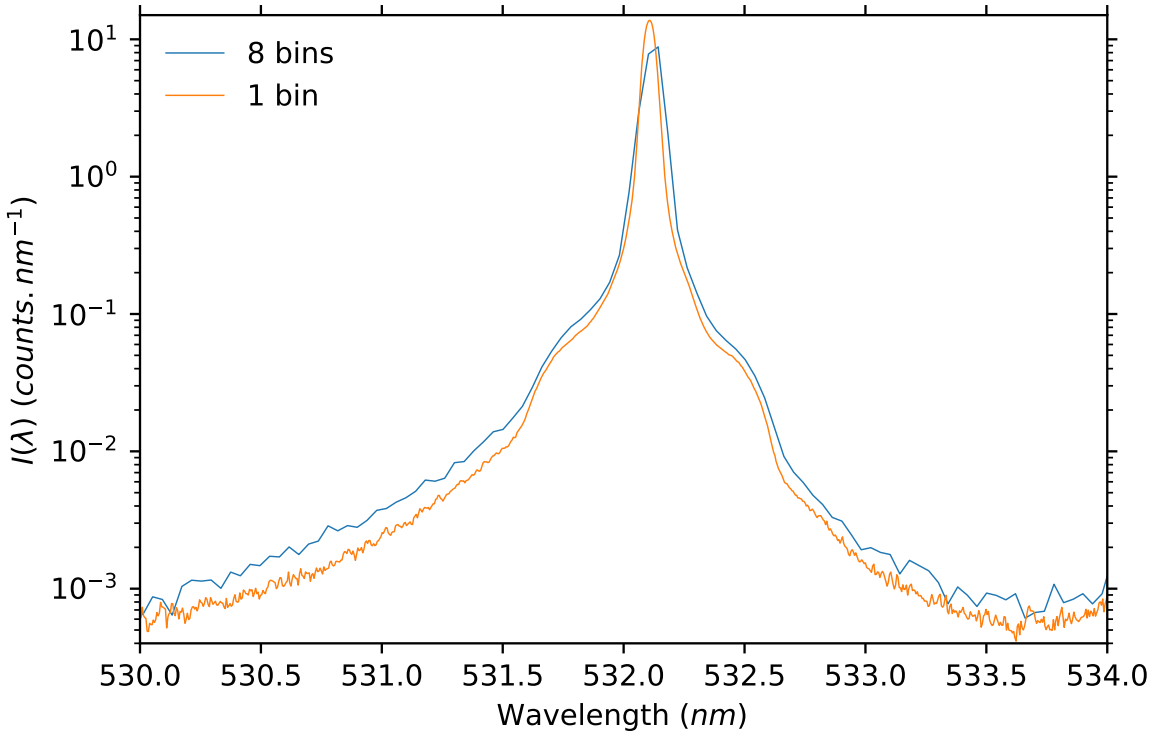

Figure 2. Instrument function profile for the THETIS diagnostic with a 300 μm spectrometer slit width, without horizontal wavelength binning and with binning over 8 horizontal pixels

B. Raman analysis for calibration

In this work, we have opted to use Raman scattering for calibration. The Raman calibration procedure, used for example in Refs. 2, 12, 44, 47, relies on fitting to rotational emission lines which are shifted with respect to the laser wavelength. For Rayleigh calibration, used for example in Refs. 34 and 30, the Rayleigh scattered signal and the diagnostic stray light are superposed at the initial laser wavelength.

A certain degree of care is required in the use of Rayleigh signals for calibration. The superposed Rayleigh and stray light signals at the incident wavelength are typically orders of magnitude higher in amplitude than the Thomson signal. Since the detector response is not usually perfectly linear with light intensity (a feature we have observed in our case, with deviations increasing at very high light intensities), there is a risk of inaccuracy when high-amplitude Rayleigh spectra are used to calibrate the weaker Thomson scattered radiation. Instead, we use Raman signals measured at pressures which give spectra of comparable amplitudes to the Thomson scattering spectra.

It should also be noted that Rayleigh calibration and Thomson spectrum setups will also differ slightly in their optical components (for example, acquiring the Rayleigh spectrum will require the removal of filters used to attenuate light at the incident wavelength); such differences between the setups must be carefully accounted for.

1. *Raman signal measurement*

The following procedure is used to obtain a typical Raman spectrum used for calibration in this work.

The vacuum vessel is filled with nitrogen to a known pressure (10 mbar) and the Bragg volume grating is initially misaligned to allow the detection of a large Rayleigh signal. This Rayleigh signal is used simply for a preliminary alignment of the detection branch. Once this alignment is complete, the Bragg grating is realigned to minimize the light peak at 532 nm.

A signal acquisition is performed with the laser traversing the vessel for 10 minutes (camera acquisition 6000 exposures/frame), followed by a noise spectrum acquisition with the laser off. This latter signal is subtracted from the first. The use of software binning of 8 pixels on the horizontal (wavelength) axis improves the signal to noise ratio by a maximum theoretical value of $\sqrt{8}$ compared to the unbinned case.

The Raman spectrum obtained under these conditions is shown in Fig. 3. This figure illustrates the good performance of the volume Bragg grating in attenuating the light at 532 nm, while permitting the Raman Stokes and anti-Stokes transitions close to the laser wavelength to be fully resolvable. We have performed similar Raman spectrum measurements over a range of pressures (0.5 - 10 mbar) and verified that the area under the Raman curves increases linearly with pressure, a condition which validates the use of such spectra in calibrations. Fig. 3 shows the experimental points (blue crosses, orange line) as well as the fit (green line, obtained after the fitting procedure described in Section 3). The blue crosses indicate data points taken into account for fitting, while the orange line passes through all the data points, including points around the laser wavelength which are excluded in fitting.

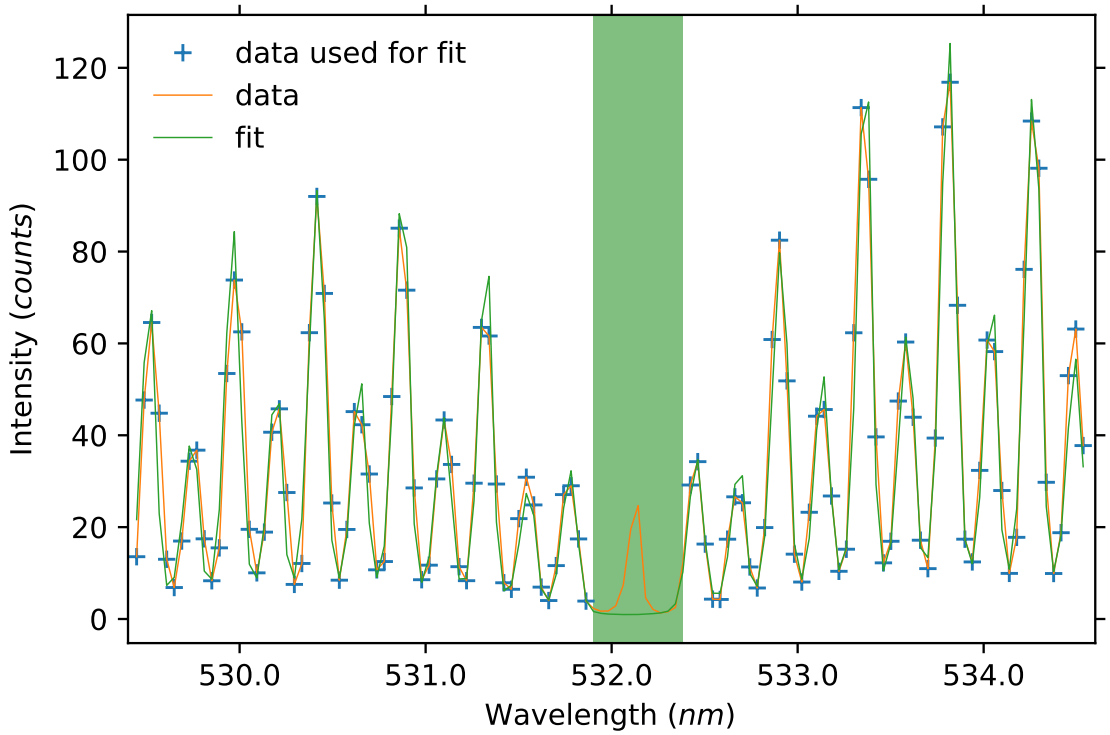

Figure 3. Raman scattering spectrum used for calibration, obtained for nitrogen at 10 mbar and a spectrometer slit width of 300 μm. The green bar at the center of the spectrum shows the region in which points are excluded from the fit.

2. *Raman spectrum distribution*

The spectral peaks seen in Fig. 3 correspond to transitions from one rotational state to another, with these states characterized by the rotational quantum number J. Only J to $J \pm 2$ transitions are authorized

($J \in N$). The expected wavelengths and line powers associated with these transitions can be predicted using analytical expressions developed in detail in other works, such as in Ref. 4. Here we summarize only a few useful forms.

The wavelengths of the different Raman peaks associated with these transitions are given by:

$$\lambda_{J\to J+2} = \lambda_i + \frac{{\lambda_i}^2}{hc}\, B(4J+6) \tag{1}$$

for Stokes transitions (occurring at shorter wavelengths than λ_i, the initial laser wavelength), and

$$\lambda_{J\to J-2} = \lambda_i - \frac{\lambda_i^2}{hc}\, B(4J-2) \tag{2}$$

for anti-Stokes transitions. The constant B is the rotational constant (2.48×10^{-4} eV for N_2).[37]

The theoretical form of the scattered Raman spectrum can be written as

$$\frac{dP_R}{d\Omega}(\lambda) = n_g P_i L \sum_{J,J'} \frac{n_J(T)}{n_g} \frac{d\sigma_{R,J\to J'}}{d\Omega} \delta(\lambda - \lambda_{J\to J'}) \tag{3}$$

where $\delta(\lambda - \lambda_{J\to J'})$ is the Dirac delta function (of value 1 for $\lambda = \lambda_{J\to J'}$, 0 for $\lambda \neq \lambda_{J\to J'}$). n_g is the gas density, P_i the incident laser power and L the length of the scattering volume. $\frac{d\sigma_{R,J\to J'}}{d\Omega}$ is the differential cross-section for a Raman transition $J \to J'$. n_J represents the density of an initial rotational state J. In Eq. 3 the natural Raman spectral width is neglected.

In Eq. 3, $\frac{d\sigma_{R,J\to J'}}{d\Omega}$ is dependent on the direction of observation, the anisotropy of the molecular polarisability tensor (known as γ), the wavelength $\lambda_{J\to J'}$ associated with a transition, and Placzek-Teller coefficients (known as $b_{J\to J'}$) associated with a transition.[37] We note here that a correct interpolation of γ^2 using the values from Ref. 37 gives a value of 0.505×10^{-48} cm^6, different from the value used in some other references. The term n_J respects Maxwell-Boltzmann statistics, therefore depending on the energy of the rotational level, its degeneracy and temperature.

n_J is dependent on a partition sum term Q (dependent on the gas temperature T and known rotational gas constant B) and a statistical weighting factor g_J.[37]

3. Raman signal fitting

The expression for the actual measured Raman signal I_{RM} takes into account certain effects: (i) the observation of light within a specific solid angle $\Delta\Omega$, (ii) the transmission τ of the system, representing the fraction of scattered light which is detected following the total optical losses associated with the detection branch and detector conversion efficiency, (iii) the redistribution of the radiation due to the instrument function $f(\lambda)$, and (iv) the discrete nature of the measured signal (due to recording by individual pixels). Taking these features into account, the measured Raman scattering spectrum is given by

$$I_{RM}(\lambda,\tau,T) = \tau n_g P_i L \delta\lambda \Delta\Omega \quad \sum_{J,J'} \frac{n_J(T)}{n_g} \frac{d\sigma_{R,J\to J'}}{d\Omega} f(\lambda - \lambda_{J\to J'}) \tag{4}$$

where $\delta\lambda$ is the wavelength step associated with one pixel. This function is fitted to the experimental data using a least-squares fitting algorithm to produce the optimized values of τ and T. The corresponding fit is shown by the green curve in Fig. 3.

C. Thomson spectral analysis

The total Thomson scattered spectrum power may be expressed generally as

$$\frac{dP_T}{d\Omega}(\lambda) = n_e P_i L \frac{d\sigma_T}{d\Omega} \frac{1}{\Delta\lambda_g\sqrt{2\pi}} e^{-\frac{(\lambda-\lambda_0)^2}{2\Delta\lambda_g^2}} d\lambda \tag{5}$$

where n_e is the electron density and $\frac{d\sigma_T}{d\Omega}$ is the Thomson scattering differential cross-section. The last term is the form factor for a Gaussian distribution of electron energies, with a Gaussian half-width (standard deviation) of $\Delta\lambda_g$ and a central wavelength of λ_0.

The actual measured Thomson spectrum I_T is given by

$$I_T(\lambda, \Delta\lambda_g, \lambda_0, n_e) = \tau n_e P_i L \delta\lambda^2 \Delta\Omega \frac{d\sigma_T}{d\Omega} \quad \int_0^{\lambda} \frac{1}{\Delta\lambda_g\sqrt{2\pi}} e^{-\frac{(u-\lambda_0)^2}{2\Delta\lambda_g^2}} \cdot f(\lambda - u)du \tag{6}$$

Eq. 6 gives an analytical form with free parameters of $\Delta\lambda_g$, λ_0 and electron density n_e. This analytical form is fitted to the experimental Thomson spectrum. The electron temperature for the data, T_e (again assuming a Maxwellian distribution) is proportional to the square of Gaussian spectrum width $\Delta\lambda_g$. T_e is given by

$$T_e = \frac{m_e c^2}{8k_B sin^2(\frac{\theta}{2})} \left(\frac{\Delta\lambda_g}{\lambda_i}\right)^2 \tag{7}$$

where k_B is Boltzmann's constant, c the light speed in a vacuum and θ the scattering angle (90° in our case).

The inclusion of the parameter τ, explicitly determined from the prior Raman spectrum curve fitting, allows the absolute value of n_e to be deduced directly from the Thomson fit. λ_0 provides an absolute measurement of the wavelength shift associated with the global electron drift; in the absence of a significant global electron velocity, $\lambda_0 = \lambda_i$.

In the application of the fit to the experimental data, care is taken to exclude the central portion of the spectrum affected by the presence of the Bragg filter (typically within a range of ± 0.25 nm around λ_i).

IV. Diagnostic preliminary implementation

A. Motivation for hollow cathode investigations

In order to validate the component choices and the diagnostic design, preliminary measurements were designed to measure electron properties of a hollow cathode source.[18] Hall thrusters, one of the sources for which the new diagnostic has been envisaged, are electric propulsion devices whose operation relies on certain fundamental aspects, including (i) the creation of a region of magnetized, energetic electrons for the ionization of entering neutral gas and the maintenance of a localized electric field for efficient ion extraction outside the device, and (ii) the neutralization of the accelerated ions. These aspects require the use of an electron source (to feed the ionization region and for recombination with ions). The hollow cathode fulfills these functions and is therefore a critical component in sources such as Hall thrusters and gridded ion engines.

This source was selected for the first tests for a number of reasons. Firstly, it is simple, compact (the cathode under study has a length of 15 cm) and offers the possibility of full access to the expanding plasma outside the device. Secondly, the expected electron densities (ranging from 10^{16} to 10^{18} m^{-3} for the plasma expanding outside the cathode orifice[38]) are on the order of what is expected in the sources for which the diagnostic has been designed. Tests on the cathode therefore serve to validate future applications of the diagnostic. Lastly, research into hollow cathodes has undergone a resurgence in recent years, due to attempts to develop cathodes suitable for emerging thruster models.[17,32] Our preliminary tests, briefly discussed in this work, represent the first time the electron temperatures and densities in cathodes have been measured by incoherent Thomson scattering.

B. Device description

The cathode studied is a device with a 3 mm orifice, operating with xenon gas, and similar to the cathode developed by the Russian MIREA institute. It uses a thermo-emissive LaB_6 disc heated by a filament. Emitted electrons ionize the input gas and the maintenance of a sheath close to the emissive disc produces a strong electric field which further increases emission and ionization. An electric field applied between the heater and the anode results in the acceleration of electrons outside the device. In Fig. 1, the anode (a metal plate) is positioned 40 mm from the cathode orifice; under such conditions the cathode is said to be operating in diode mode. In standard operation of the cathode with a thruster, the anode is situated at the rear of the thruster channel. Nominal operating parameters of this device are a discharge current of 5 A and a gas flow rate of 4 sccm. During experiments the vacuum vessel operating pressure is typically 2 - 4 $\times$ 10^{-5} mbar. Fig. 1 shows the setup for cathode experiments, in which the position of the laser line is maintained and the cathode translated in the x direction for axial investigations of the electron properties.

Cathode operation is known to be characterized by two modes: the "spot" and "plume" modes.[11] The spectra shown in this work focus on the spot mode, with higher density and less-pronounced discharge current oscillations. Experiments are carried out with the same parameters described earlier in the Raman calibration procedure.

C. Thomson scattering experiments

Two examples (high and low scattered signal amplitudes) have been chosen to illustrate typical results for the cathode Thomson scattering measurements.

Figs. 4 and 5 show the Thomson scattering spectra obtained for two respective operating points for the cathode: (i) at 16 A discharge current and 8 sccm (spot mode) at an axial position 1.3 mm from the cathode orifice, and (ii) at 2 A, 8 sccm (spot mode) at 8 mm from the cathode orifice. As before, the blue crosses and orange line show the experimental data, and the green rectangle shows the zone for which the experimental points are ignored for the curve fitting.

For Fig. 4, a Gaussian fit to the experimental data gives corresponding values of electron temperature and density of, respectively, 2.27 ± 0.18 eV and 9.41 ± 0.75 × 10^{17} m^{-3}. The value of V_{ar} shown on the figure is the square of the signal standard deviation, calculated over all the points used for the fit (in units of $counts^2$), which can be regarded as an expression of the signal power.

Fig. 5 shows a noisier signal (with much lower variance) to which Gaussian fitting is still applicable. The figure shows the Thomson signal (top) and the corresponding noise signal (bottom). For Fig. 5, the corresponding values of electron temperature and density are, respectively, 0.46 ± 0.05 eV and 1.8 ± 0.2 × 10^{16} m^{-3}. The ratio of the variances in this figure providess an idea of the diagnostic sensitivity: for the given acquisition parameters and for a ratio of V_{ar} of the Thomson/noise signals of 2.5, the measured electron density is on the order of 10^{16} m^{-3} for an electron temperature below 1 eV.

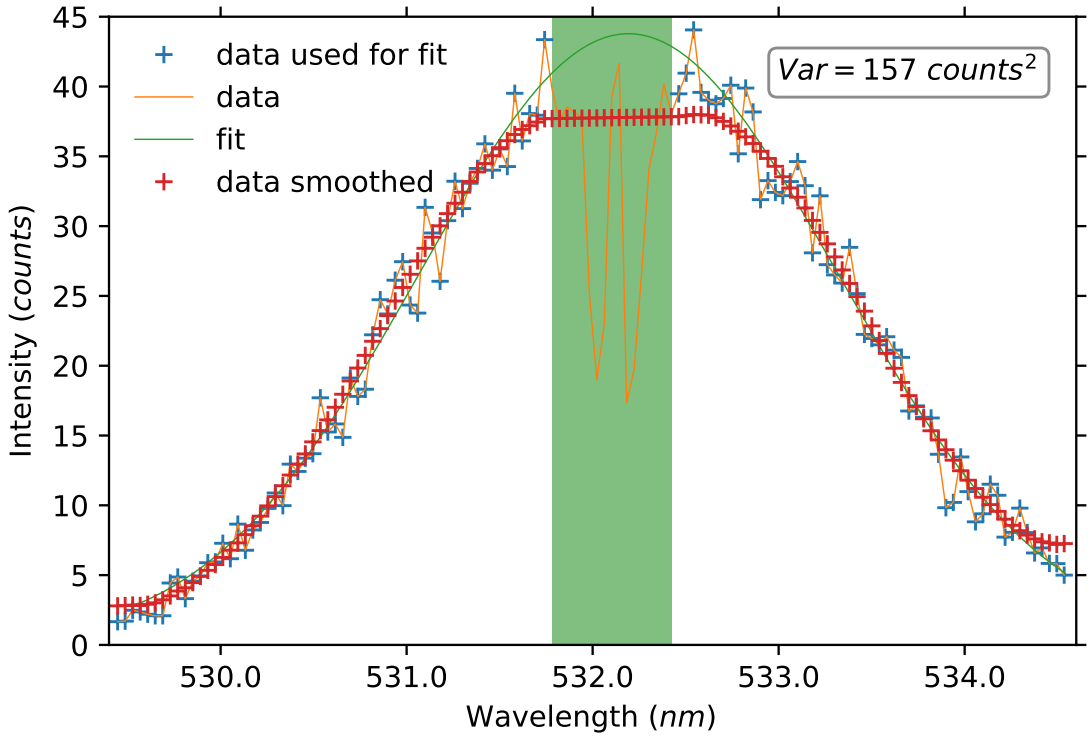

Figure 4. Thomson scattering spectrum obtained for a Xe plasma at 1 mm from a hollow cathode orifice, for 16 A discharge current and 8 sccm gas flow rate (spot mode)

On the basis of these results, a number of comments may be made:

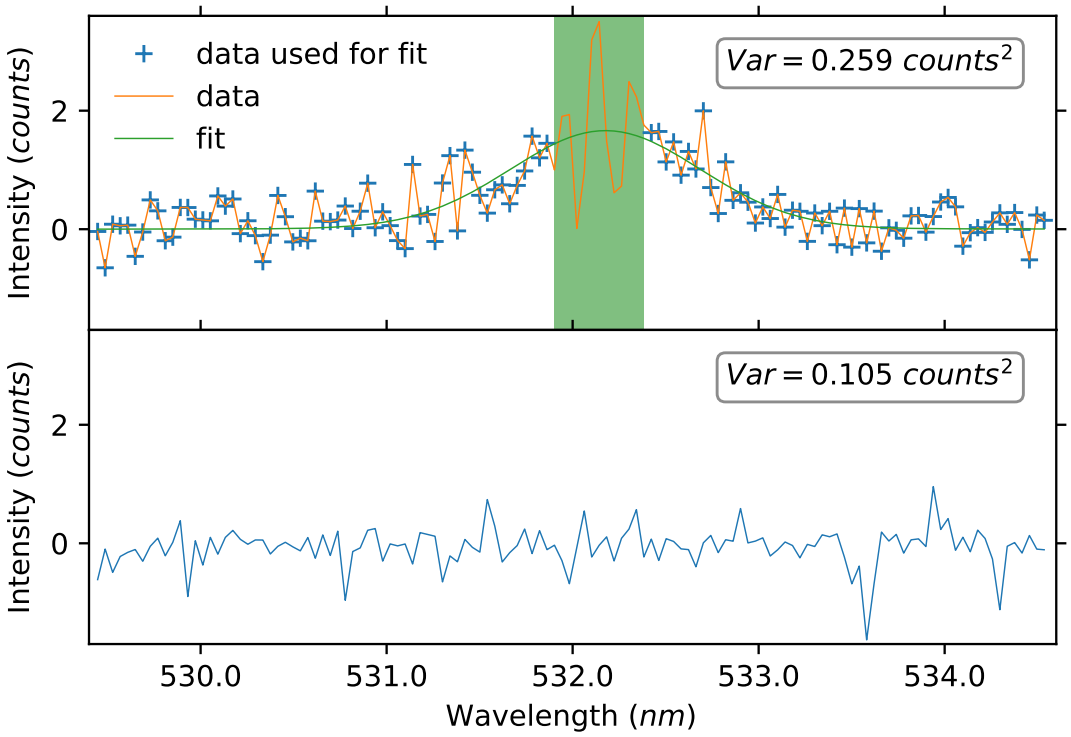

Figure 5. Thomson scattering spectrum obtained for a Xe plasma at 8 mm from a hollow cathode orifice, for 2 A discharge current and 8 sccm gas flow rate (spot mode). The top figure shows the Thomson spectrum and the bottom figure the corresponding noise spectrum

(i) For these measurements, the performance of the Bragg filter is excellent, even for measurements close to the metallic cathode orifice (Fig. 4). The narrowness of the bandstop region makes the resolution of low electron temperatures (below 0.5 eV) possible, while the filter sufficiently attenuates the stray light at 532 nm to allow the spectrum to be correctly fitted. Measurements have been performed at a shortest distance of 1 mm between the probing laser beam and the cathode orifice. The electron temperatures on the order of a few eV are on the same order as those expected for this cathode in numerical simulations.[38]

(ii) The low densities measurable, for example, for signals such as that shown in Fig. 5, are on the same order as those measurable using the most sensitive diagnostics currently available (capable of resolving densities down to 10^{16} m^{-3}). It is worth noting that in these preliminary measurements, the acquisition duration has been limited to 10 minutes; the signal to noise ratio can be further reduced by increasing the horizontal binning and/or increasing the acquisition duration. In Section F, avenues for improving the diagnostic sensitivity further are summarized.

(iii) The signal acquisition duration covers several periods of discharge current oscillations, which indicates that the measured electron properties are averaged over these oscillations. We have measured very low discharge current fluctuations in the spot mode of 2% (discharge current standard deviation/mean discharge current). However, in the operation of other sources such as the Hall thruster, discharge current fluctuations of close to 100% are encountered in certain regimes. For such measurements, time resolution of the electron properties will be critical. This will be done using signal accumulation triggered at fixed points in the phase of stabilized discharge current oscillations.

D. Electron velocity and energy distribution functions

The expression of Thomson scattering data using the EVDF (or EEDF) is of particular value when the distribution of electron energies cannot be characterized purely with a Gaussian spectrum shape[22] (in which

case it is associated with a single electron temperature). This is true of cases in which the distribution of energies is non-Maxwellian. The use of the EVDF or EEDF provides a fuller depiction of the spread in electron energies arising, for example, due to particle heating by plasma turbulence (producing high-energy tails of distribution functions) or energy losses (resulting in truncated distribution functions). In future implementations of the diagnostic on other sources, we intend to focus on studying such deviations. In this section, we describe the procedures used to plot the EVDF and EEDF for the Gaussian spectrum of Fig. 4.

The wavelength shift $\Delta\lambda$ corresponding to a spread in electron energies can be expressed as a velocity shift v,

$$v = \frac{c\Delta\lambda}{\lambda_i \sin(\theta/2)} \tag{8}$$

The normalized electron velocity distribution function is expressed as

$$f(v) = -\frac{\frac{dI}{d\lambda}\Delta\lambda}{\Sigma(\frac{dI}{d\lambda}\Delta\lambda\delta v)} \tag{9}$$

where δv is the velocity shift associated with the wavelength step ($\delta\lambda$) corresponding to one pixel. $\frac{dI}{d\lambda}$ as the derivative of the Thomson-scattered spectral intensity $I(\lambda)$ with respect to λ. The experimental data of the Thomson scattered spectrum are first smoothed (in our case, using a Savitzky-Golay algorithm). The points corresponding to this smoothing are depicted by red crosses in Fig. 4. The derivative $\frac{dI}{d\lambda}$ is then applied to the smoothed data.

The corresponding form of the EVDF is shown in Fig. 6, for the side of the symmetric Thomson spectrum for which $\lambda > \lambda_i$. As for Fig. 4, the excluded region of points is indicated by a green rectangle.

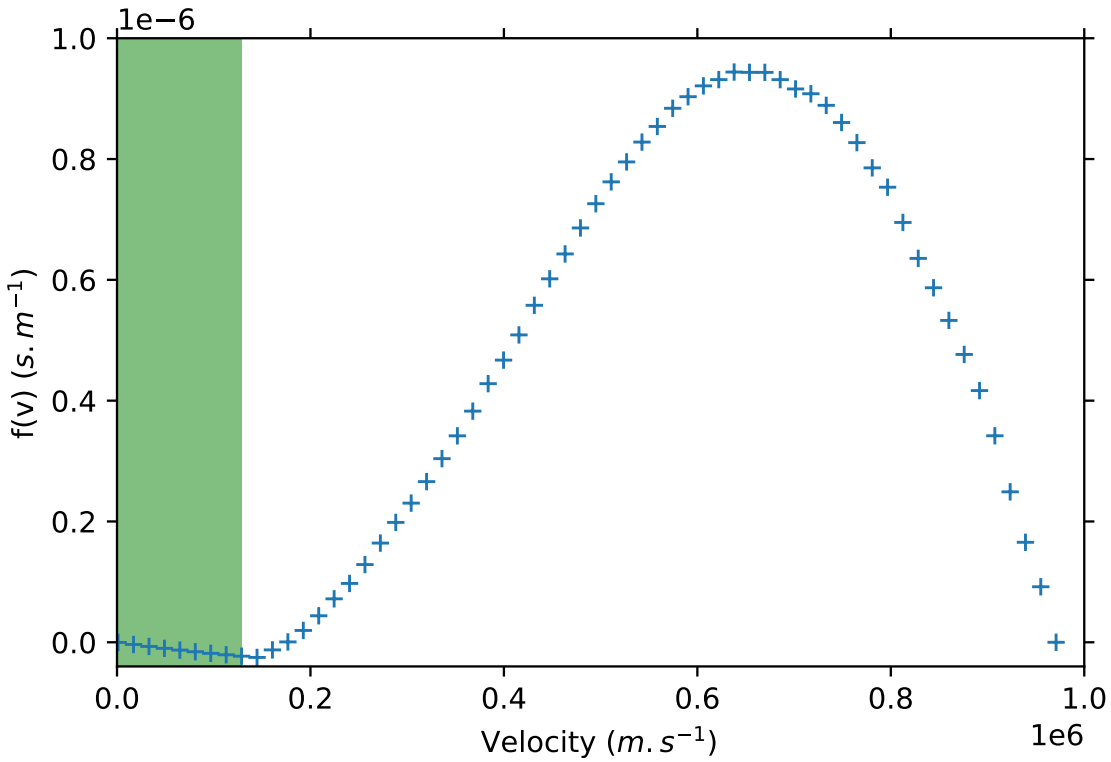

Figure 6. Electron velocity distribution function (EVDF) for data shown in Fig. 4 ($\lambda > \lambda_i$)

Similarly, the spread in electron energies may be shown using the EEDF (via the relation for the energy shift $\Delta E = \frac{1}{2} m_e \Delta v^2$, where m_e is the electron mass).

The normalized EEDF $f(E)$ is written

$$f(E) = -\frac{\frac{dI}{d\lambda} sgn(\Delta\lambda)}{\Sigma(\frac{dI}{d\lambda}\delta E)} \tag{10}$$

where δE is the energy step associated with a single pixel. The EEDF corresponding for the side of the symmetric Thomson spectrum of Fig. 4 for which $\lambda > \lambda_i$ is shown in Fig. 7. No notable deviation from a Maxwellian shape is seen.

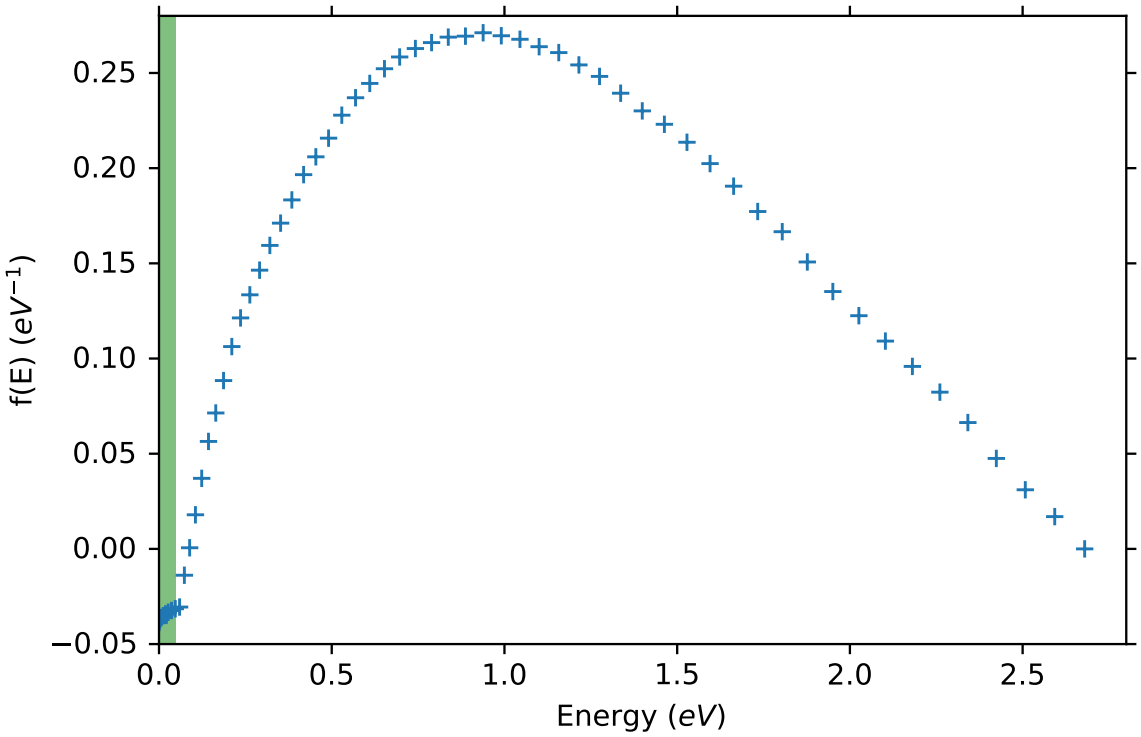

Figure 7. Electron energy distribution function (EEDF) for data shown in Fig. 4 ($\lambda > \lambda_i$)

E. Measurement uncertainties

The uncertainties associated with the measurement of the n_e and T_e are due to a number of points. Fluctuations in the laser power introduce an uncertainty on the order of 1%, and the uncertainty due to pressure gauge response is 0.5%. There is an uncertainty due to the quality of the Gaussian fit to the experimental data and this is computed by determining a covariance matrix at the time of fitting; this uncertainty depends on the signal to noise ratio and can be dominant for low-amplitude scattered signals. The largest source of uncertainty for large-amplitude scattered signals, however, is associated with the uncertainty of the value of the Raman cross-sections used for fitting; this is 8%.[37]

F. Planned diagnostic upgrades

A number of steps have been identified to further lower the detection limit, and these adaptations will be made over the course of the next few months. The first is the use of a new camera with a Gen III intensifier with a higher quantum efficiency (50% at 532 nm) and a back-illuminated iCCD to improve the signal to noise ratio. The use of recently-developed emiCCD detectors is another possibility. Such detectors allow for single photon detection and this would be valuable in experiments in which electrons of very high energies are present but low in number. The excellent linearity of response of these detectors, in comparison to

standard iCCDs, over a large range of signal intensities also suggests that we may safely implement Rayleigh calibration at high signal levels, without risking calibration errors for the Thomson signal.

Another planned upgrade is the use of a larger volume Bragg grating; in the current setup, fully half of the collected power arriving at the filter is not transmitted to the spectrometer because it falls outside the filter dimensions. It may also be necessary to use a stack of two of such filters when larger levels of stray light are expected; such an arrangement would still provide lower losses than a triple-grating spectrometer.

V. Conclusions

A new compact incoherent Thomson scattering diagnostic known as THETIS has been designed, constructed and validated. The attractiveness of the diagnostic lies in its combination of sensitivity and compactness; the use of a volume Bragg grating for the first time in ITS studies results in reduced transmission losses, in comparison to diagnostics using triple grating spectrometers for stray light reduction. Recent advances in the development of such volume Bragg gratings offer a means of improving the flexibility and range of applications for ITS diagnostics. In this work, preliminary measurements made on a hollow cathode plasma demonstrate high diagnostic sensitivity (measurements of electron densities on the order of 10^{16} m^{-3}) and planned upgrades are expected to further enhance the diagnostic capability. The diagnostic is intended for a range of implementations on low-temperature plasma sources, including planar magnetrons, Hall thrusters and electron cyclotron resonance sources. Studies with the new THETIS bench will be paired with coherent scattering measurements made with the recently-developed PRAXIS diagnostic. These implementations will provide highly-detailed information regarding both electron properties and dynamics.

VI. Acknowledgments

The authors would like to express their gratitude to members of the SACM team of CEA/Saclay (J. Schwindling and O. Tuske). The contributions of G. Largeau, L. Peilleron and E. Labrude, and advice from P. Bernhard and H. J. van der Meiden, were also appreciated. The authors would also like to acknowledge support from the French Space Agency (CNES).

References

[1]L. A. Artsimovich, G. A. Bobrovsky, E. P. Gorbunov, D. P. Ivanov, V. D. Kirillov, E. I. Kuznetsov, S. V. Mirnov, M. P. Petrov, K. A. Razumova, V. S. Strelkov, and D. A. Scheglov. *Plasma Physics and Controlled Fusion Research (IAEA)*, CN24/B1:157, 1969.

[2]L. P. Bakker, J. M. Freriks, F. J. de Hoog, and G. M. W. Kroesen. *Rev. Sci. Instrum.*, 71:2007, 2000.

[3]D. R. Bates, A. E. Kingston, and R. W. P. McWhirter. *Proc. R. Soc. Lond. A*, 267:297, 1962.

[4]P. F. Bernath. *Spectra of Atoms and Molecules*. Oxford University Press, 2005.

[5]M. D. Bowden, Y. Goto, H. Yanaga, P. J. A. Howarth, K. Uchino, and K. Muraoka. *Plasma Sources Sci. Technol.*, 8:203, 1999.

[6]M. D. Bowden, M. Kogano, Y. Suetome, T. Hori, K. Uchino, and K. Muraoka. *J. Vac. Sci. Technol. A*, 17:493, 1999.

[7]E. A. D. Carbone, S. Hübner, J. M. Palomares, and J. J. A. M. van der Mullen. *J. Phys. D: Appl. Phys.*, 45:345203, 2012.

[8]E. A. D. Carbone, J. M. Palomares, S. Hübner, E. Iordanova, and J. J. A. M. van der Mullen. *J. Inst.*, 7:C01016, 2012.

[9]J. Cavalier, N. Lemoine, G. Bonhomme, S. Tsikata, C. Honoré, and D. Grésillon. *Phys. Plasmas*, 20:082107, 2013.

[10]D. L. Crintea, U. Czarnetzki, S. Iordanova, I. Koleva, and D. Luggenhölscher. *J. Phys. D: Appl. Phys.*, 42:045208, 2009.

[11]G. A. Csiky. *AIAA 7th Electric Propulsion Conference, Williamsburg, Virginia, USA, AIAA 60-258.*

[12]J. M. de Regt, R. A. H. Engeln, F. P. J. de Groote, J. A. M. van der Mullen, and D. C. Schram. *Rev. Sci. Instrum.*, 66:3228, 1995.

[13]V. M. Donnelly. *J. Phys. D: Appl. Phys.*, 37:R217, 2004.

[14]U. Fantz. *Plasma Sources Sci. Technol.*, 15:S137, 2006.

[15]A. Friss and A. Yalin. *AIAA Propulsion and Energy Forum, 53rd AIAA/SAE/ASEE Joint Propulsion Conference, 10-12 July 2017, Atlanta, Georgia, USA, AIAA 2017-4792.*

[16]D. H. Froula, S. H. Glenzer, N. C. Luhmann Jr., and J. Sheffield. *Plasma Scattering of Electromagnetic Radiation: Theory and Measurement Techniques*. Academic Press, 2011.

[17]D. M. Goebel and E. Chu. *32nd International Electric Propulsion Conference, 11 - 15 September, Wiesbaden, Germany, 2011-053.*

[18]D. M. Goebel, R. M. Watkins, and K. K. Jameson. *J. Propul. Power*, 23:552, 2007.

[19]H. R. Griem. *Principles of Plasma Spectroscopy*. Cambridge University Press, 1997.

[20]A. Guthrie and R. K. Wakerling. *The Characteristics of Electrical Discharges in Magnetic Fields*. McGraw Hill, 1949.

[21]X. Han, C. Shao, X. Xi, J. Zhao, Z. Qing, J. Yang, X. Dai, and K. Shinichiro. *Rev. Sci. Instrum.*, 84:053502, 2013.

[22]M. Huang, K. Warner, S. Lehn, and G. M. Hieftje. *Spectrochim. Acta B*, 55:1397, 2000.

[23]I. H. Hutchinson. *Principles of Plasma Diagnostics*. Cambridge University Press, 2001.

[24]Yu. M. Kagan and V. I. Perel'. *Sov. Phys. Uspekhi*, 81:767, 1963.

[25]M. Yu Kantor, A. J. H. Donné, R. Jaspers, H. J. van der Meiden, and TEXTOR Team. *Plasma Phys. Control Fusion*, 51:055002, 2009.

[26]P. J. Kelly and R. D. Arnell. *Vacuum*, 56:159, 2000.

[27]B. L. M. Klarenaar, F. Brehmer, S. Welzel, H. J. van der Meiden, M. C. M. van de Sanden, and R. Engeln. *Rev. Sci. Instrum*, 86:046106, 2015.

[28]J. Lasalle and P. Platz. *Appl. Optics*, 18:4124, 1979.

[29]H. M. Mott-Smith and I. Langmuir. *Phys. Rev.*, 28:727, 1926.

[30]K. Muraoka and A. Kono. *J. Phys. D: Appl. Phys.*, 44:043001, 2011.

[31]G. Neumann, U. Bänziger, M. Kammeyer, and M. Lange. *Rev. Sci. Instrum.*, 64:19, 1993.

[32]F. Nürmberger, A. Hock, and M. Tajmar. *AIAA 7th Propulsion and Energy Forum, 51st AIAA/SAE/ASEE Joint Propulsion Conference, 27 - 29 July, Orlando, Florida, USA, 2015-3822*.

[33]M. Paillet, F. Meunier, M. Verhaegen, S. Blais-Ouellette, and R. Martel. *Rev. Sci. Instrum*, 81:053111, 2010.

[34]J. M. Palomares, E. I. Iordanova, A. Gamero, A. Sola, and J. J. A. M. v. d. Mullen. *J. Phys. D: Appl. Phys.*, 43:395202, 2010.

[35]R. Pasqualotto, P. Nielsen, C. Gowers, M. Beurskens, M. Kempenaars, T. Carlstrom, D. Johnson, and JET-EFDA contributors. *Rev. Sci. Instrum.*, 75:3891, 2004.

[36]N. J. Peacock, D. C. Robinson, M. J. Forrest, P. D. Wilcock, and V. V. Sannikov. *Nature*, 224:488, 1969.

[37]C. M. Penney, R. L. St. Peters, and M. Lapp. *J. Opt. Soc. Am.*, 64:712, 1973.

[38]G. Sary. *Modélisation d'une cathode creuse pour propulseur à plasma*. Ph.D. thesis, Université de Toulouse 3 Paul Sabatier, Toulouse, France, 2016.

[39]B. H. Seo, S. J. You, and J. H. Kim. *Jpn. J. Appl. Phys.*, 54:086102, 2015.

[40]S. Tsikata, N. Lemoine, V. Pisarev, and D. Grésillon. *Phys. Plasmas*, 16:033506, 2009.

[41]S. Tsikata and T. Minea. *Phys. Rev. Lett.*, 114:185001, 2015.

[42]R. Turner and T. O. Poehler. *J. Appl. Phys.*, 39:5726, 1968.

[43]O. Tuske, G. Adroit, O. Delferrière, D. De Menezes, Y. Gauthier, R. Gobin, and F. Harrault. *Rev. Sci. Instrum.*, 79:02B710, 2008.

[44]M. J. van de Sande, R. H. M. Deckers, F. Lepkojus, W. Buscher, and J. J. A. M. van der Mullen. *Plasma Sources Sci. Technol.*, 11:466, 2002.

[45]M. C. M. van de Sanden, G. M. Janssen, J. M. de Regt, D. C. Schram, J. A. M. van der Mullen, and B. van der Sijde. *Rev. Sci. Instrum.*, 63:3369, 1992.

[46]H. J. van der Meiden, R. S. Al, C. J. Barth, A. J. H. Donné, R. Engeln, W. J. Goedheer, B. de Groot, A. W. Kleyn, W. R. Koppers, N. J. Lopes Cardozo, M. J. van de Pol, P. R. Prins, D. C. Schram, A. E. Shumack, P. H. M. Smeets, W. A. J. Vijvers, J. Westerhout, G. M. Wright, and G. J. van Rooij. *Rev. Sci. Instrum.*, 79:013505, 2008.

[47]A. F. H. van Gessel, E. A. D. Carbone, P. J. Bruggeman, and J. J. A. M. van der Mullen. *Plasma Sources Sci. Technol.*, 21:015003, 2012.

[48]R. L. Washeleski. *Laser Thomson scattering measurements of electron temperature and density in a Hall-effect plasma*. Ph.D. thesis, Michigan Technological University, Michigan, USA, 2013.

[49]N. Yamamoto, K. Tomita, N. Yamasaki, T. Tsuru, T. Ezaki, Y. Kotani, K. Uchino, and H. Nakashima. *Plasma Sources Sci. Technol.*, 19:045009, 2010.

[50]V. V. Zhurin, H. R. Kaufman, and R. S. Robinson. *Plasma Sources Sci. Technol.*, 8:R1, 1999.